Journal of Nuclear Materials 627 (2026) 156626

Contents lists available at ScienceDirect

Journal of Nuclear Materials

journal homepage: www.elsevier.com/locate/jnucmat

First-principles study on the structural stability, radiation effect, and disorder-induced strengthening in A-site high-entropy spinel $(Zn_{0.25}Mn_{0.25}Ca_{0.25}Mg_{0.25})Al_2O_4$

Haowen Guo [a,b,c], Xiaoyi Xia [a,b,c], Yuntao Yang [a,b,c], Chenguang Liu [a,b,c,*], Qing Peng [d], Yuhong Li [e], Fei Gao [f]

[a] College of Nuclear Equipment and Nuclear Engineering, Yantai University, Yantai 264005, Shandong, China
[b] Shandong Key Laboratory of Special Metallic Materials for Nuclear Equipment, Yantai University, Yantai 264005, Shandong, China
[c] Yantai Key Laboratory of Advanced Nuclear Energy Materials and Irradiation Technology, Yantai University, Yantai 264005, Shandong, China
[d] Power and Mechanical Engineering, Wuhan University, Wuhan 430072, China
[e] School of Nuclear Science and Technology, Lanzhou University, Lanzhou 730000, China
[f] Nuclear Engineering & Radiological Sciences, University of Michigan, Ann Arbor, MI 48109, USA

ARTICLE INFO

Keywords:
High-entropy spinel
First principles
Mechanical properties
Radiation resistance

ABSTRACT

High-entropy spinel oxides (HESOs) exhibit exceptional properties, and selective cation site occupancy can significantly influence their structures and behaviors. In this study, the special quasi-random structure (SQS) method combined with density functional theory (DFT) was employed to model and analyze the A-site high-entropy spinel $(Zn_{0.25}Mn_{0.25}Ca_{0.25}Mg_{0.25})Al_2O_4$ and its various possible cation configurations. The transformation from normal to inverse spinel demonstrates a gradual order-disorder transition, accompanied by increased configurational entropy. Calculations reveal that HESOs are thermodynamically stable, with negative formation energies and favorable Gibbs free energy changes upon synthesis. Analysis of cation antisite defect formation energies and Al-vacancy migration barriers suggests enhanced resistance to amorphization. Furthermore, as the degree of disorder increases, both elastic moduli and hardness improve while anisotropy decreases. These findings elucidate the connection between structural disorder and mechanical strengthening, offering valuable guidance for the design of HESOs for use in extreme environments.

1. Introduction

The rapid proliferation of energy-intensive technologies, such as Artificial Intelligence (AI), has driven an unprecedented surge in global electricity demand [1]. As a cornerstone of the clean energy transition, nuclear energy remains one of the most viable and sustainable power sources in the global energy landscape [2]. However, the advancement of next-generation nuclear systems imposes increasingly stringent requirements on structural materials, necessitating exceptional thermal stability, enhanced radiation tolerance, and superior structural integrity under extreme service conditions. Consequently, a profound understanding and accurate prediction of radiation-induced damage are imperative for optimizing the performance and safety of both current and future nuclear reactors.

Magnesium aluminate spinel ($MgAl_2O_4$) exhibit exceptional mechanical stability, chemical durability, and radiation resistance, rendering them promising candidates for applications in inert matrix fuels [3–5], radiofrequency (RF) window materials for fusion reactors [6,7], and immobilization matrices for radioactive waste [8,9]. Research has demonstrated that $MgAl_2O_4$ spinel can withstand fast neutron or heavy-ion irradiation doses up to 250 dpa without undergoing amorphization at temperatures above 300 K. Even at a cryogenic temperature of 100 K under 400 keV Xe ion irradiation, the amorphization threshold remains as high as 25 dpa [10]. Furthermore, under high-dose neutron and light-ion irradiation, the material exhibits only minimal swelling [11–13]. Under irradiation conditions, the recombination of Mg^{2+} and Al^{3+} ions with vacancies or the exchange of Mg^{2+} and Al^{3+} ions on their respective lattice sites will be readily accommodated [14]. Since cation antisite defects possess the lowest formation energy, the irradiation damage energy is ultimately deposited within the crystal in

* Corresponding author.
E-mail address: liuchg@ytu.edu.cn (C. Liu).

https://doi.org/10.1016/j.jnucmat.2026.156626
Received 1 December 2025; Received in revised form 6 March 2026; Accepted 27 March 2026
Available online 28 March 2026

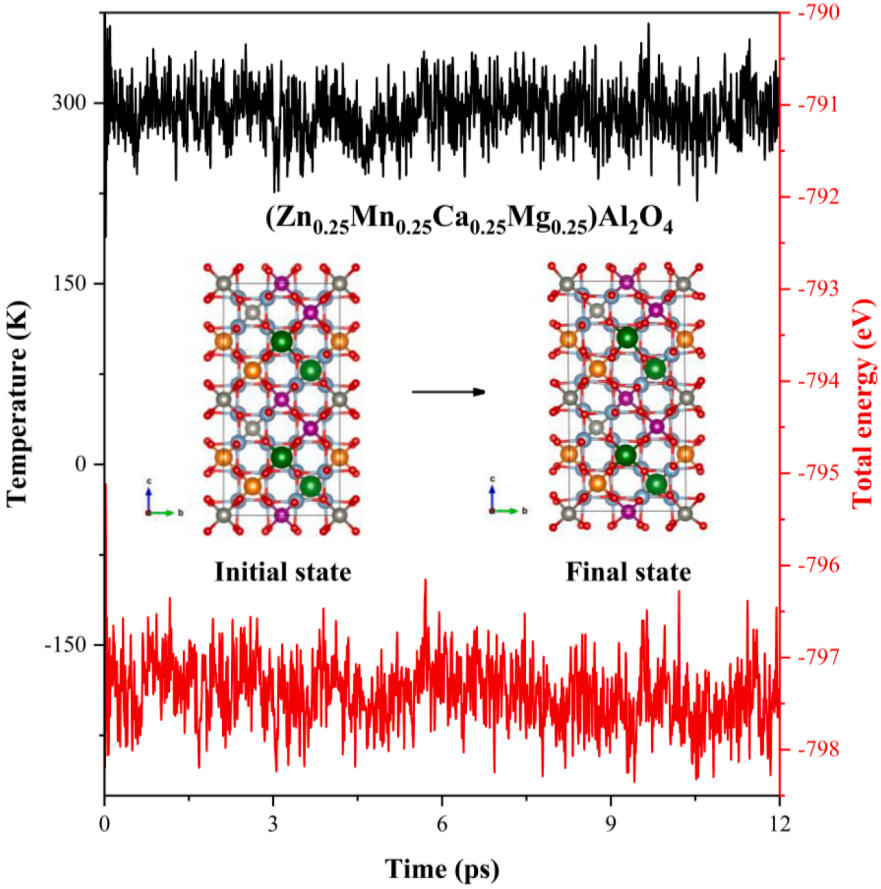

Fig. 1. Time-dependent total energy trajectories spanning the initial-to-final state transition for $(Zn_{0.25}Mn_{0.25}Ca_{0.25}Mg_{0.25})Al_2O_4$.

the form of cation disorder [10,15]. Similar to many other ceramic materials, the capacity of complex oxides to accommodate such disorder is intrinsically linked to their amorphization resistance [16–18]. Consequently, cation antisite defect is the primary response mechanism of spinels to irradiation [3,11,19–21]. This radiation tolerance originates predominantly from the accommodation of point defects via cation antisite defect, while preserving mechanical stability [11,17,22]. The cation sublattices of all spinel crystals naturally exhibit a certain degree of disorder. Under irradiation, the concentration of antisite defects in $MgAl_2O_4$ increases further. Moreover, radiation induced cation vacancy-interstitial Frenkel pairs participate in highly efficient and harmless recombination, a process known as lattice self-healing [11,17,23–25]. Under irradiation, spinels undergo a phase transition from ordered state to disordered state and eventually to defective rocksalt structure [26]. The abundance of vacancies within the disordered rocksalt phase provides sufficient space for cation reordering. The complex oxides can maintain radiation tolerance through defect migration mechanisms [27,28]. Given that migration frequency is directly dictated by the migration barrier, higher defect mobility promotes radiation recovery by accelerating the recombination process [24]. Due to the unique configuration of the spinel cation sublattice, vacancy defects significantly influence radiation resistance. For instance, the non-stoichiometric $MgO{\cdot}2.4(Al_2O_3)$ spinel, which possesses a higher vacancy concentration, exhibits superior radiation performance compared to its stoichiometric counterpart [14,29,30]. Additionally, anion vacancies act as defect recombination centers, playing a constructive role in the structural recovery process [26].

High-entropy materials (HEMs) have been demonstrated to exhibit superior radiation resistance, showing great potential for broad applications in the nuclear energy sector [31]. The inherent chemical complexity of HEMs modulates the generation, interaction, and interstitial-vacancy recombination processes of initial radiation-induced defects by altering defect formation energies, migration barriers, and diffusion pathways [32–34]. In high-entropy alloys (HEAs), point defects and defect clusters experience a rugged potential energy landscape, which significantly enhances defect recombination [35]. Similarly, the lower cation antisite formation energy in high-entropy MAX phases suggests a greater ability to maintain lattice integrity, leading to enhanced amorphization resistance [36]. In high-entropy pyrochlores (HEPOs), lower antisite formation energies facilitate the annihilation of Frenkel pairs (FPs) by promoting cation antisite formation at both A and B sites [37]. Furthermore, the reduced defect migration barriers in high-entropy ceramics promote defect recombination, thereby resulting in superior anti-amorphization capabilities [38,39].

However, the mechanisms by which chemical disorder influences defect properties and subsequently dictates the amorphization resistance of high-entropy spinel (HES) ceramics remain unclear. In this study, we employ first-principles calculations to investigate the impact of chemical disorder on HES defect characteristics. Specifically, we systematically analyze the structural and energetic properties of A-site HES across varying degrees of inversion to capture the effects of this disorder. Because point defect kinetics govern the defect recombination rate [24], migration barriers are further evaluated to provide deeper insights into defect evolution. Beyond radiation resistance, the mechanical prosperity of nuclear waste forms is crucial for preventing cracking during cooling or accidental handling [40]. Therefore, by calculating the mechanical properties of HES, we highlight its potential as a robust matrix for immobilizing high-level radioactive waste under extreme conditions. Finally, because local bonding characteristics fundamentally govern mechanical behavior [41], we examine the underlying electronic properties to elucidate the physical origins of the observed mechanical variations.

Table 1
The degree of inversion α, lattice constant a (Å), formation energy E_f (eV/atom), mixing enthalpy ΔH_{mix} (kJ·mol^{-1}) and configurational entropy ΔS_{conf} (J·mol^{-1}·K^{-1}) calculated from the structural models with varied degrees of cation antisite disorder. For clarity, the different models were designated by short names.

Short name	Composition of model	α	a (Å)	E_f (eV/atom)	ΔH_{mix} (kJ·mol^{-1})	ΔS_{conf} (J·mol^{-1}·K^{-1})
pristine	$(Zn_{0.25}Mn_{0.25}Mg_{0.25}Ca_{0.25})Al_2O_4$	0	8.277	-2.347	-6.468	34.577
1-1	$(Zn_{0.25}Mn_{0.25}Mg_{0.25}Al_{0.25})(Ca_{0.125}Al_{0.875})_2O_4$	0.125	8.213	-2.331	-1.139	40.842
1-2	$(Zn_{0.25}Mn_{0.25}Ca_{0.25}Al_{0.25})(Mg_{0.125}Al_{0.875})_2O_4$	0.125	8.159	-2.339	-3.863	40.842
1-3	$(Zn_{0.25}Ca_{0.25}Mg_{0.25}Al_{0.25})(Mn_{0.125}Al_{0.875})_2O_4$	0.125	8.180	-2.283	15.196	40.842
1-4	$(Ca_{0.25}Mn_{0.25}Mg_{0.25}Al_{0.25})(Zn_{0.125}Al_{0.875})_2O_4$	0.125	8.168	-2.329	-0.362	40.842
2-1	$(Zn_{0.25}Mg_{0.25}Al_{0.5})(Ca_{0.125}Mn_{0.125}Al_{0.75})_2O_4$	0.25	8.151	-2.26	23.074	43.928
2-2	$(Mn_{0.25}Mg_{0.25}Al_{0.5})(Ca_{0.125}Zn_{0.125}Al_{0.75})_2O_4$	0.25	8.199	-2.296	10.773	43.928
2-3	$(Ca_{0.25}Mn_{0.25}Al_{0.5})(Mg_{0.125}Zn_{0.125}Al_{0.75})_2O_4$	0.25	8.198	-2.317	3.804	43.928
2-4	$(Ca_{0.25}Mg_{0.25}Al_{0.5})(Mn_{0.125}Zn_{0.125}Al_{0.75})_2O_4$	0.25	8.136	-2.278	16.740	43.928
2-5	$(Zn_{0.25}Ca_{0.25}Al_{0.5})(Mg_{0.125}Mn_{0.125}Al_{0.75})_2O_4$	0.25	8.278	-2.27	19.584	43.928
2-6	$(Zn_{0.25}Mn_{0.25}Al_{0.5})(Ca_{0.125}Mg_{0.125}Al_{0.75})_2O_4$	0.25	8.210	-2.31	5.991	43.928
3-1	$(Mg_{0.25}Al_{0.75})(Ca_{0.125}Zn_{0.125}Mn_{0.125}Al_{0.625})_2O_4$	0.375	8.171	-2.222	35.733	45.577
3-2	$(Ca_{0.25}Al_{0.75})(Zn_{0.125}Mn_{0.125}Mg_{0.125}Al_{0.625})_2O_4$	0.375	8.152	-2.246	27.494	45.577
3-3	$(Zn_{0.25}Al_{0.75})(Ca_{0.125}Mn_{0.125}Mg_{0.125}Al_{0.625})_2O_4$	0.375	8.237	-2.274	18.16	45.577
3-4	$(Mn_{0.25}Al_{0.75})(Ca_{0.125}Zn_{0.125}Mg_{0.125}Al_{0.625})_2O_4$	0.375	8.268	-2.287	13.915	45.577
4-1	$Al(Mg_{0.125}Ca_{0.125}Zn_{0.125}Mn_{0.125}Al_{0.5})_2O_4$	1	8.123	-2.232	32.234	46.103

2. Method

All first-principles calculations were performed using the Vienna Ab-initio Simulation Package (VASP) [42,43] based on density functional theory (DFT) and the projector augmented wave (PAW) method [44]. The exchange-correlation interactions were described using the generalized gradient approximation (GGA) parameterized by Perdew-Burke-Ernzerhof (PBE) [45]. A plane-wave cutoff energy of 520 eV was adopted, and a 2 × 2 × 2 Monkhorst-Pack *k*-point mesh was used for Brillouin zone sampling of the 56-atom high-entropy spinel oxide (HESO) supercell. For structural optimizations, all atomic positions were fully relaxed until the total energy converged to 10^{-6} eV/atom and the total force was converged to 0.015 eV/Å. To ensure higher precision in the calculations of elastic constants and electronic structures, stricter convergence criteria were applied, with total energy and forces converged to 10^{-7} eV/atom and 0.001 eV/Å, respectively. To correct for the self-interaction errors associated with strongly correlated *d* electrons in transition metal ions, the Hubbard *U* correction was applied within the GGA+U framework. The effective *U* values ($U_{eff} = U\text{-}J$) were set to 3.9 eV for Mn [46]. To model different degrees of cation antisite disorder in $(Zn_{0.25}Mn_{0.25}Ca_{0.25}Mg_{0.25})Al_2O_4$, special quasi-random structure (SQS) structures were generated using the Alloy Theoretic Automated Toolkit (ATAT) [47]. In all models, metal cations were distributed randomly at A-site and the anion sublattice was fully occupied by oxygen atoms.

Ab-initio molecular dynamics (AIMD) simulations were also performed using VASP to assess the dynamic stability of the HESO structures. A higher plane wave energy cutoff of 600 eV was employed, along with a Γ-centered 1 × 1 × 1 *k*-point mesh. To ensure accurate calculations, a 2 × 1 × 1 supercell of the $(Zn_{0.25}Mn_{0.25}Ca_{0.25}Mg_{0.25})Al_2O_4$ containing 112 atoms was employed for the AIMD simulations. The calculations employed the *NPT* ensemble and the temperature was controlled at 300 K using the Langevin thermostat [48], which stochastically couples the system to a heat bath and ensures efficient and correct sampling of the canonical distribution. The atomic positions and lattice parameters were treated as dynamic variables. The equations of motion were integrated with a time step of 3 fs for a total simulation time of 12 ps (4000 steps) to make sure adequate sampling of the relevant phase space. Dynamics visualizations were generated using VESTA [49], enabling detailed analysis of structures.

Mechanical properties were calculated through the energy-strain method with a series of strains (±0.005, ±0.010, and ±0.015) utilizing the VASPKIT toolkit [50]. The Born-Huang criterion [51] was applied to assess the mechanical stability, and the elastic moduli of all systems were derived using the Voigt-Reuss-Hill (VRH) approximation. The Poisson's ratio (ν) was calculated using $\nu = (E/2\,G)\text{-}1$ [52], while the Pugh's ratio (k) was obtained from $k = G/B$ [53]. Additionally, the Vickers hardness was estimated through Chen's model employing the equation $H_v = 2(k^2G)^{0.583}–3$ [54].

3. Results

3.1. Assessment of synthesis feasibility

The structural stability and synthesis feasibility of $(Zn_{0.25}Mn_{0.25}Ca_{0.25}Mg_{0.25})Al_2O_4$ were comprehensively evaluated through AIMD simulations, formation energy, and Gibbs free energy analyses. AIMD simulation was conducted at 300 K for 12 ps to assess the thermal stability of the high-entropy spinel structure. As shown in Fig. 1, the atomic positions of $(Zn_{0.25}Mn_{0.25}Ca_{0.25}Mg_{0.25})Al_2O_4$ remained nearly unchanged throughout the entire simulation, with only minor thermal vibrations observed around equilibrium positions. The absence of significant total energy fluctuations confirms the structural robustness and thermal stability of the HESO in ambient conditions.

To further evaluate the thermodynamic feasibility of synthesizing $(Zn_{0.25}Mn_{0.25}Ca_{0.25}Mg_{0.25})Al_2O_4$, the formation energies were calculated using density functional theory (DFT) combined with the special quasi-random structure (SQS) approach. Although the convex-hull method is generally preferred for assessing the phase stability of multicomponent materials [55–57], the complexity of the $(Zn_{0.25}Mn_{0.25}Ca_{0.25}Mg_{0.25})Al_2O_4$ phase space makes such a treatment intractable. Therefore, in this study, the formation energy was adopted as a practical and informative descriptor to provide a preliminary assessment of the synthesizability of the high-entropy spinel [58]. The formation energy of $(Zn_{0.25}Mn_{0.25}Ca_{0.25}Mg_{0.25})Al_2O_4$, relative to the convex hull constructed from a linear combination of oxide precursor energies, defines its hull distance [56]. The overall chemical reaction can be expressed as:

$$\frac{1}{4}ZnO + \frac{1}{4}MgO + \frac{1}{4}CaO + \frac{1}{4}MnO + Al_2O_3 \rightarrow (Zn_{0.25}Mn_{0.25}Ca_{0.25}Mg_{0.25})Al_2O_4 \quad (1)$$

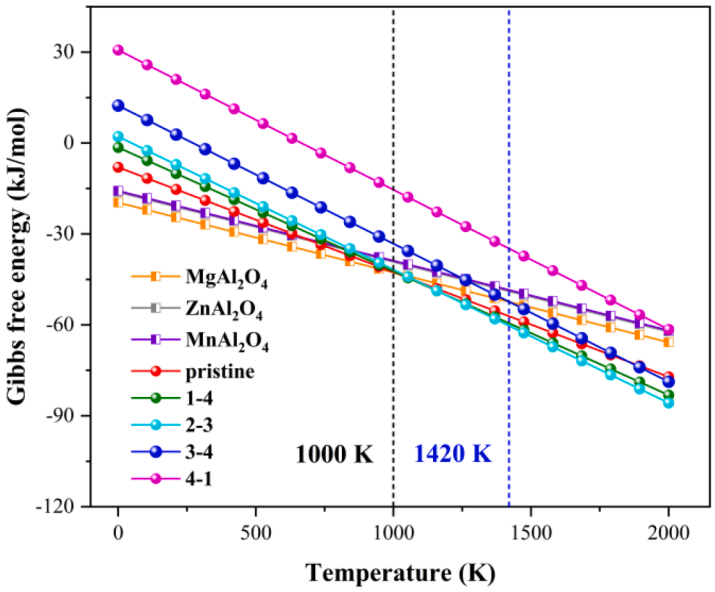

Fig. 2. Thermodynamic analysis of possible chemical reactions occurring during the synthesis of high-entropy spinels selected under experimental conditions, which were designated by short names in Table 1.

The formation energy per atom was calculated as [59,60]:

$$E_{form} = \frac{(E_{tot} - \sum N_i E_i)}{\sum N_i} \quad (2)$$

where E_{tot} is the total energy of HESO per supercell, E_i is the energy of one of the ith-type atoms in the stable primary crystal structure or the molecular phase (for oxygen), and N_i is the number of the ith-type atoms in the supercell. All configurations, from the pristine to the fully antisite-disordered structures, exhibit negative formation energies with only slight variations (Table 1), suggesting that they are thermodynamically stable. Among them, the pristine configuration $(Zn_{0.25}Mn_{0.25}Ca_{0.25}Mg_{0.25})Al_2O_4$ possesses the lowest formation energy, indicating the highest synthesis likelihood. According to Emery *et al.*, compounds with hull distances smaller than approximately 100 meV per atom are considered synthesizable [56]. Therefore, HESO is predicted to be experimentally formable. For high-entropy spinels, the enthalpy of mixing (ΔH_{mix}) reflects the process of solid-solving various metal atoms into the spinel lattice sites. Interestingly, our results show that the ΔH_{mix} for the 3–1 and 4–1 systems is significantly higher than that of other systems. This observation can be attributed to two main factors. First, the thermodynamic stability of the cation distribution plays a crucial role. As shown in Fig. 4, Zn, Mn, Ca, and Mg atoms thermodynamically prefer to occupy the A-sites. The atomic configurations of the 3–1 and 4–1 systems, however, are thermodynamically unstable and demand extra energy input, leading to their maximum energetic instability. Furthermore, this instability is significantly exacerbated by the severe lattice distortion inherent to these two systems. As shown in Fig. 4, the four metal atoms (Zn, Mn, Ca, and Mg) are inherently more stable when occupying the A-sites. In the 3–1 system, cations with high antisite defect formation energies (Mn, Ca, and Mg) are forced to exchange positions with Al at the B-sites. This configuration is thermodynamically unfavorable and requires additional energy to drive the cation inversion, leading to the observed energetic instability, a similar mechanism applies to the 4–1 system. Secondly, the elevated ΔH_{mix} is closely related to the severe lattice distortion in these two systems. To quantify, we calculated the average atomic radial displacement (Å) and lattice mismatch δ [61]. Compared to the pristine system (0.051 and 0.072 Å), the radial displacements of metal and oxygen atoms are notably larger in both the 3–1 (0.073 and 0.219 Å) and 4–1 (0.075 and 0.221 Å) configurations. Notably, the distortion in 4–1 is greater than in 3–1, which is consistent with the trend in their mixing enthalpies ΔH_{mix}. This is further supported by the lattice mismatch (%): 4–1 (5.734) > 3–1 (5.514) > Pristine (2.573).

High-entropy spinel oxides (HESOs) are typically synthesized as stable single-phase solid solutions within the temperature range of 700–1000 °C, where high temperature solid-state synthesis remains the most commonly employed method. Other high-entropy oxide ceramics, such as high-entropy pyrochlores, are typically synthesized from binary oxide precursors via high-temperature solid-state reactions. Zhu *et al.* successfully synthesized these high-entropy pyrochlores within the corresponding temperature range, as confirmed by both theoretical calculations and experimental validation [62]. To further evaluate the synthetic feasibility of HESO, all possible chemical reactions involved in the formation of various cation configurations were analyzed. Based on the DFT-relaxed energies at 0 K, the thermodynamic stability of HESO configurations with varying degrees of cation disorder was systematically assessed. Under high-temperature solid-state experimental conditions, the Gibbs free energy of each possible reactions, $\Delta G^{\theta}_{R,T}$, can be expressed as a function of temperature. The representative reactions for the formation of single-component and high-entropy spinels are presented in expressions 3, 5, 7 and 9, and their corresponding Gibbs free energy can be calculated using expression 4, 6, 8 and 10.

$$MgO + Al_2O_3 \rightarrow MgAl_2O_4 \quad (3)$$

$$\Delta G^{\theta}_{R,T} = \Delta G^{(a)}_{mix} \quad (4)$$

$$MnO + Al_2O_3 \rightarrow MnAl_2O_4 \quad (5)$$

$$\Delta G^{\theta}_{R,T} = \Delta G^{(b)}_{mix} \quad (6)$$

$$ZnO + Al_2O_3 \rightarrow ZnAl_2O_4 \quad (7)$$

$$\Delta G_{R,T}^{\theta} = \Delta G_{mix}^{(c)} \tag{8}$$

$$\frac{1}{4}\mathrm{ZnO} + \frac{1}{4}\mathrm{MgO} + \frac{1}{4}\mathrm{CaO} + \frac{1}{4}\mathrm{MnO} + \mathrm{Al_2O_3} \rightarrow \left(\mathrm{Zn_{0.25}Mn_{0.25}Ca_{0.25}Mg_{0.25}}\right)\mathrm{Al_2O_4} \tag{9}$$

$$\Delta G_{R,T}^{\theta} = \Delta G_{mix}^{(d)} \tag{10}$$

where $\Delta G_{mix}^{(n)}$ denotes the mixing Gibbs free energy of chemical reaction (n), which can be calculated using the following expression [63]:

$$\Delta G_{mix}^{(n)} = \Delta H_{mix}^{(n)} - T\Delta S_{mix}^{(n)} \tag{11}$$

where $\Delta H_{mix}^{(n)}$, $\Delta S_{mix}^{(n)}$, and T represent the mixing enthalpy, mixing entropy, and temperature, respectively.

The calculated mixing enthalpy [64], $\Delta H_{mix}^{(n)}$, is given by the following expression:

$$\Delta H_{mix} = \frac{E_{tot} - \sum n_k E_k^{MO}}{\sum n_k} \tag{12}$$

Where E_{tot} is the total energy of the HESO and E_k^{MO} denotes the energy of each binary oxide component.

For high-entropy systems, the mixing entropy is primarily dominated by the configurational entropy (S_{conf}). The concept of high-entropy oxides (HEOs) was originally developed as an extension of high-entropy alloys (HEAs) [65]. However, the calculation methods for the configurational entropy of solid solutions are not yet standardized. This challenge arises primarily because the high-entropy concept was first established in metallic alloy, which generally possess simple crystal structures with cations occupying a single type of lattice site. In contrast, high-entropy oxides such as spinels and perovskites contain multiple cation sublattices, rendering the configurational entropy analysis considerably more complex. Zhu *et al.* incorporated the configurational entropy contribution from intrinsic vacancies when evaluating the thermodynamic stability of high-entropy pyrochlores [62]. For spinels, under specific conditions: high-energy particle irradiation or local charge imbalance, the intrinsic Octahedral vacant sites (*16c*) within the spinel lattices may become partially occupied [14,66,67]. Based on this consideration, we propose that the intrinsic vacancies in the cation sublattice of spinels also contribute to the overall configurational entropy. Accordingly, a modified approach for calculating the configurational entropy of spinels is proposed as follows:

$$S_{conf} = -R\left[x\left(\sum_{a=1}^{M} x_a \ln x_a\right)_{A-site} + y\left(\sum_{b=1}^{N} y_b \ln y_b\right)_{B-site} + z\left(\sum_{o=1}^{P} z_o \ln z_o\right)_{O-site} + S_{conf-vac}\right] \tag{13}$$

where x_a, y_b and z_o are the mole fractions of species at the A-site, B-site and O-site, respectively. While M, N and P are the number of cations present on A-site, B-site and anions on O-site, respectively. For an oxide system, S_{conf} from O-site is ideally zero. $S_{conf-vac}$ accounts for the contribution of intrinsic octahedral cation vacancies to the configurational entropy.

The calculated variation of ΔG_{mix} with temperature (0–2000 K) is shown in Fig. 2. According to the theory of phase formation in multi-component systems, both positive and negative ΔH_{mix} values inhibit the formation of solid solutions, while ΔH_{mix} close to favor random cation distribution and phase stability [68]. Based on this criterion, the high-entropy spinel configurations with ΔH_{mix} values closest to zero were selected for further analysis. As can be seen from the Fig. 2, all reactions exhibit a monotonically decreasing $\Delta G_{R,T}^{\theta}$ with increasing temperature, indicating an increased thermodynamic driving force at higher temperature. Among the three single-component spinels, $MgAl_2O_4$ shows the lowest $\Delta G_{R,T}^{\theta}$, implying the strongest driving force for its formation. Therefore, during the synthesis of high-entropy spinels, $MgAl_2O_4$ formation competes most strongly with the target high-entropy spinel phase. The intersection points between $\Delta G_{R,T}^{\theta}$ of the candidate high-entropy spinel configurations and that of $MgAl_2O_4$ provides a reference for the feasible synthesis temperature. When the temperature exceeds approximately 1000 K, the driving force for the formation of high-entropy spinels surpasses that of $MgAl_2O_4$, suggesting

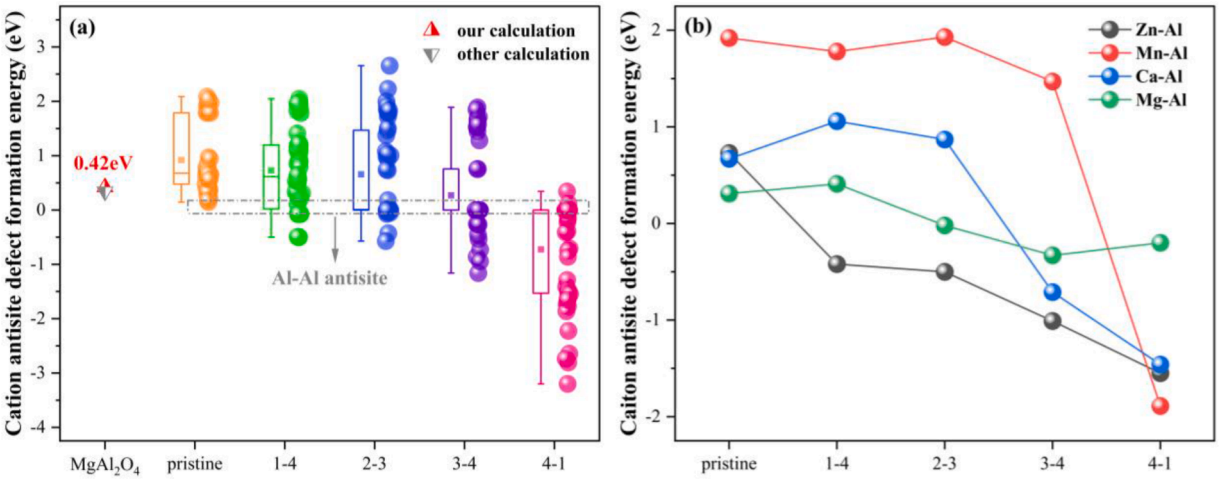

Fig. 3. a Box-plot distribution of the cation antisite defect formation energies of high-entropy spinels with varying degrees of disorder (Short name was explained in Table 1). The cation antisite defect formation energy of $MgAl_2O_4$ spinel (the red triangle) and other calculated result (the gray triangle) [69]. b The average cation antisite defect formation energis for each cation antisite pair M-Al (M=Zn, Mn, Ca and Mg) of high-entropy spinels.

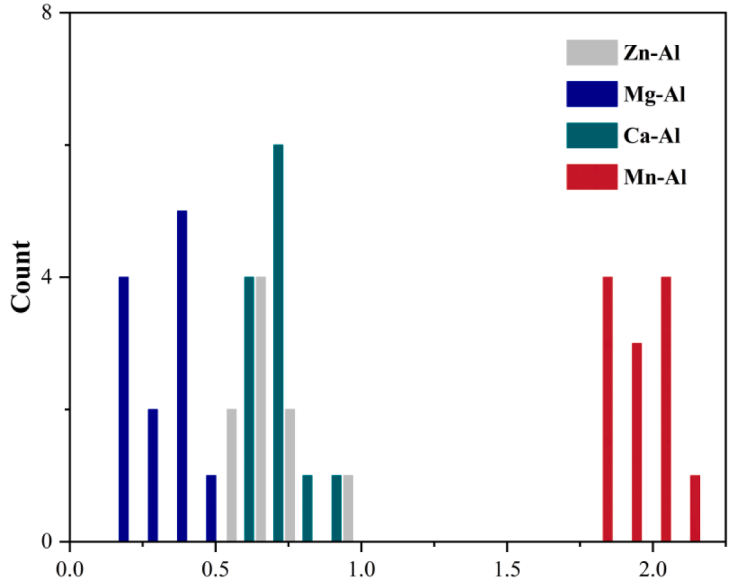

Fig. 4. The histogram of all cation antisite defect formation energies in $(Zn_{0.25}Mn_{0.25}Mg_{0.25}Ca_{0.25})Al_2O_4$ (pristine).

that the synthesis of high-entropy spinels is thermodynamically favorable above this threshold. Specifically, five configurations, $(Zn_{0.25}Mn_{0.25}Mg_{0.25}Ca_{0.25})Al_2O_4$ (pristine), $(Ca_{0.25}Mn_{0.25}Mg_{0.25}Al_{0.25})(Zn_{0.125}Al_{0.875})_2O_4$ (1–4), $(Ca_{0.25}Mn_{0.25}Al_{0.5})(Mg_{0.125}Zn_{0.125}Al_{0.75})_2O_4$ (2–3), and $(Mn_{0.25}Al_{0.75})(Ca_{0.125}Zn_{0.125}Mg_{0.125}Al_{0.625})_2O_4$ (3–4), exhibit intersections with the $\Delta G^{\theta}_{R,T}$ of $MgAl_2O_4$, within a synthesis window of 1000–1420 K. In complex multicomponent systems, phase separation behavior is primarily governed by enthalpic effects. This tendency is especially pronounced at lower temperatures, where the contribution of configurational entropy is limited and enthalpy dominates the phase evolution between single-phase and multiphase states. However, increasing $\Delta S^{(n)}_{mix}$ can effectively reduce the Gibbs free energy, providing a viable approach to counterbalance the unfavorable enthalpic contributions and enhance phase stability. This explains why the 4–1 composition exhibits the highest reference synthesis temperature (not displayed in the Fig. 2), which can be attributed to the largest enthalpic penalty among the compared systems. Therefore, the preparation of these five high-entropy spinel oxide ceramics via high-temperature solid-state reaction is thermodynamically feasible combining the analyses of formation energies and Gibbs free energies.

3.2. Cation antisite defect and vacancy migration energy

Spinel oxides are well known for their excellent radiation tolerance. Previous studies have demonstrated that the cation antisite defect formation energy (E_f^{anti}) is strongly correlated with the resistance to radiation-induced amorphization [22]. A higher E_f^{anti} indicates that the cation sublattices are more resistant to disordering under irradiation, thereby enhancing the amorphization resistance. In this work, the cation antisite defect formation energy of spinels was calculated using:

$$E_f^{anti} = E_{tot}^{anti} - E_{tot} \tag{14}$$

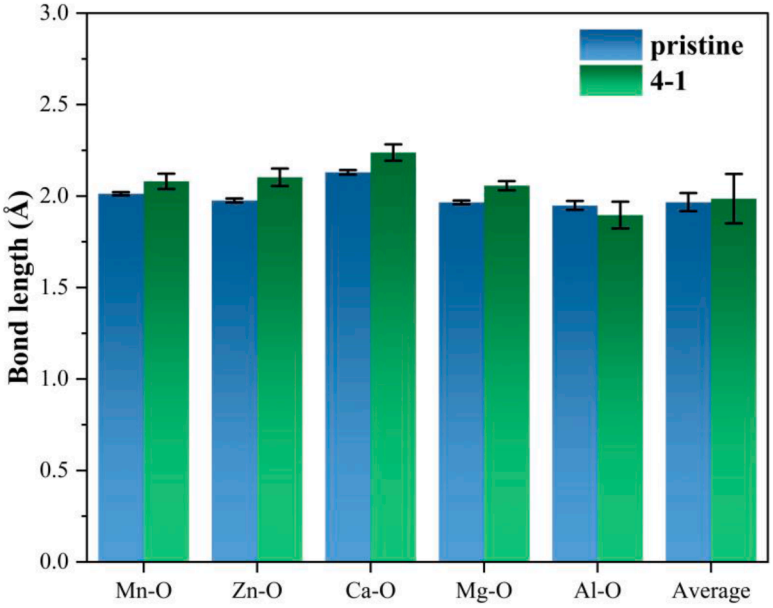

Fig. 5. The distribution of M-O (M=Mn, Zn, Ca, Mg and Al) bond lengths for both tetrahedral and octahedral coordination environments, pristine denotes the M-O bond in tetrahedral coordination, 4–1 refers to the M-O bond in octahedral coordination, and Average represents the mean M-O bond length.

Table 2
Bader charge transfer of the four A-site cations in tetrahedral and octahedral coordination environments. Charge-Tet and Charge-Oct denote the Bader charges of cations in tetrahedral and octahedral sites, respectively, and Δe represents the charge difference between the two coordination states.

	Mn	Zn	Ca	Mg
Charge-Tet	1.400	1.180	1.365	1.466
Charge-Oct	1.248	1.194	1.320	1.476
|Δe| (%)	10.82	1.20	3.30	0.68

Where, E_{tot}^{anti} represents the total energy of the spinel supercell containing a cation antisite defect, generated by exchanging the nearest-neighbor A-site and B-site cations. E_{tot} is the total energy of the perfect spinel supercell without defects. For the five selected high-entropy spinel configurations, along with the reference $MgAl_2O_4$, the calculated cation antisite defect formation energies are summarized in Fig. 3, together with the corresponding reference values.

The cation antisite defect formation energies of all high-entropy spinel structures exhibit a relatively broad distribution, which can be attributed to the complex local chemical environments inherent in high-entropy systems. With increasing antisite content (from pristine to the 4–1 configuration), the average formation energy gradually decreases. This trend arises mainly because the Al-Al exchange between the A and B sublattices has a particularly low formation energy (the gray rectangular box in Fig. 3a), approaching zero, which reduces the overall average. Another critical factor is that the antisite defect formation energy for cation pairs that have already undergone inversion is negative. This does not signify structural instability [69], rather, these configurations maintain the spinel framework following structural relaxation. On the contrary, this suggests that disordered cation pairs induced by irradiation possess a spontaneous tendency to revert to an ordered state, which represents the global energy minimum, namely, the normal spinel structure. Consequently, the A-site high-entropy spinel under irradiation damage exhibits a robust thermodynamic driving force to maintain its structural integrity. Under extreme conditions, the radiation tolerance of this structure is partially attributed to its superior capacity to accommodate cation disorder, thereby facilitating lattice self-healing [11,17,22]. Previous studies have demonstrated that the disordering tendency in spinel oxides is directly correlated with the inversion chemical energy [70] (i.e., the energetic cost of exchanging cations within the ordered lattice). For instance, Blas *et al.* found that the amorphization resistance of spinels with varying B-site compositions is proportional to the energy of their disordered states [22]. Similarly, Liu *et al.* reported that Sr-doping in $MgAl_2O_4$ reduces the cation antisite formation energy, which in turn diminishes the material's resistance to irradiation-induced amorphization [69], a phenomenon potentially linked to the percolation effect [17] in the spinel lattice. Among all investigated configurations, the pristine displays the highest average antisite defect formation energy (0.92 eV), significantly exceeding those of other high-entropy spinel configurations. Notably, this value is also substantially higher than that of single-component $MgAl_2O_4$ (0.42 eV), underscoring the superior resistance to amorphization performance of A-site high-entropy spinels compared to MAS.

Since the pristine configuration exhibits the highest defect formation energy, we further classified the antisite pair types according to their energies to elucidate the relationship between antisite pair types and antisite defect formation energies, as shown in Fig. 4. Among the four types of antisite pairs, the Mn-Al pair exhibits the highest average defect formation energy (1.92 eV), whereas the Zn-Al and Ca-Al pairs show comparable values of 0.73 eV and 0.67 eV, respectively. The Mg-Al antisite pair has the lowest defect formation energy of 0.31 eV. In general, the formation energy of cation antisite defects is correlated with the electronegativity difference between the exchanged cations, with larger differences leading to higher formation energies. However, this correlation is not strictly observed in the present high-entropy spinel system. For instance, the Ca-Al pair has the largest electronegativity difference (0.61), yet its formation energy is not the highest. This observation suggests that electronegativity difference alone cannot fully explain the antisite defect formation behavior. All antisite pairs investigated correspond to the exchange of an A-site cation from a tetrahedral site with a B-site Al atom from an octahedral site. This site exchange alters the local coordination environment, inducing charge redistribution that directly affects the defect formation energy. More charge redistribution

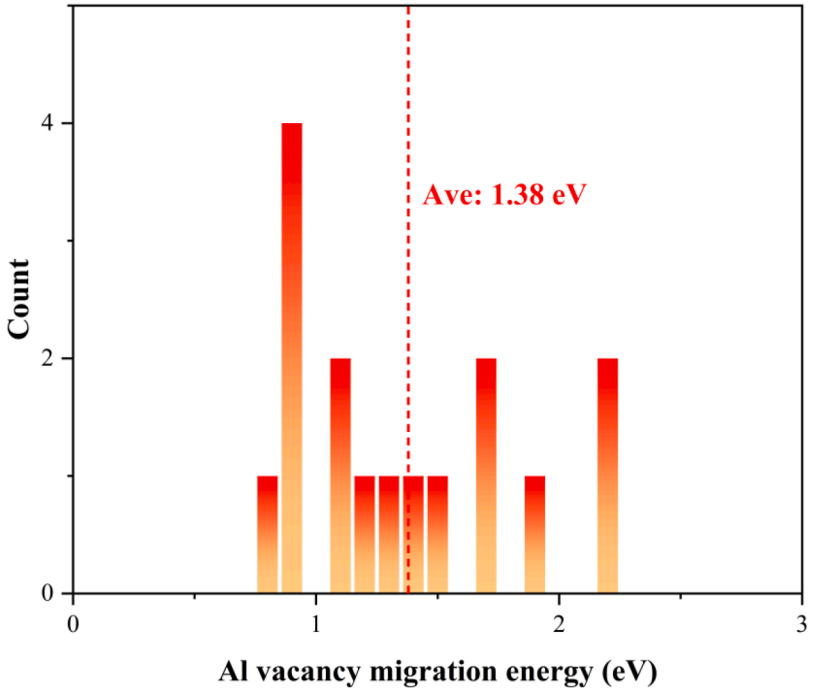

Fig. 6. The migration energy barriers of Al vacancies in the $(Zn_{0.25}Mn_{0.25}Mg_{0.25}Ca_{0.25})Al_2O_4$ (pristine). The average migration energy is indicated in the graph by a gray dashed line and corresponding text annotation.

Table 3
Overview of mechanical and elastic properties of single-component spinels and HESO selected (Short name was explained in Table 1), including Elastic constants C_{ij} (GPa), Moduli B, G, E (GPa), Pugh's ratio G/B, Poisson's ratio ν, Cauchy Pressure C_{12}-C_{44}, Vickers hardness H_V (GPa), and Zener anisotropy index A_Z. Previous calculated (Cal) and experimental (Exp) data is also compiled for comparison.

Systems	C_{11}	C_{12}	C_{44}	B	G	E	G/B	ν	C_{12}-C_{44}	H_v	A_z
$ZnAl_2O_4$	285.2	145.5	137	192.1	104.5	265.4	0.54	0.27	8.5	11.8	2.0
$MnAl_2O_4$	253.2	149	107.3	183.7	80.3	210.3	0.44	0.31	42.3	6.8	2.0
Cal [74]	248.3	148	108								
$MgAl_2O_4$	259	148.1	142.5	185	97.6	249.1	0.53	0.28	5.6	10.7	2.6
Cal [69]	270.9	160.4	146.1	197.2	99	254.3	0.50	0.29			2.6
Cal [75]	258	144	143	182	99	251					
Exp [76]	286.3	157.2	153.5	200.3							
Pristine	244.4	146.8	108.5	179.4	78.7	206	0.44	0.31	38.3	6.8	2.2
1-4	234.7	146.2	106.6	175.7	74.9	196.8	0.43	0.31	39.6	6.2	2.4
2-3	244.2	140	100.2	174.7	77.1	201.6	0.44	0.31	40.2	6.7	1.9
3-4	270.2	132.6	116.9	178.5	94.5	241.0	0.53	0.28	15.7	10.5	1.7
4-1	280.9	138.7	121.2	186.1	97.8	249.8	0.53	0.28	17.5	10.7	1.7

imposes a larger energetic penalty. Since all antisite configurations involve Al migration from octahedral to tetrahedral sites, the variations among different A-site cations become particularly significant. To further clarify this effect, the M-O (M=Mn, Zn, Ca, Mg and Al) bond lengths under different coordination environments were analyzed, as presented in Fig. 5, providing direct insight into the relationship between local bonding and antisite defect energetics.

The results indicate that the four metal cations exhibit varying degrees of M-O bond length expansion when transitioning from tetrahedral to octahedral coordination, primarily due to the larger spatial volume of octahedral sites. Among them, Mn shows the most pronounced change, with the average Mn-O bond length increasing from 2.013 Å at *8a* sites to 2.180 Å at *16c* sites, corresponding to an 8.30 % increase. Zn follows, with an increase from 1.976 Å to 2.113 Å (6.93 %), whereas Mg displays the smallest relative variation. These bond length changes exhibit a clear correlation with the formation energies of cation antisite defects. To further elucidate the influence of coordination environment changes on defect energetics, the variations in Bader charges were calculated as summarized in Table 2. Mn undergoes the largest change in Bader charge, while the other three cations display similar variations. This observation is consistent with our bond length analysis. The magnitude of cation antisite defect formation energy is highly associated with charge redistribution. Mn undergoes the most significant charge rearrangement when transitioning from tetrahedral to octahedral coordination, as reflected by its pronounced bond length variation, which in turn leads to the highest formation energy for the Mn-Al antisite defect. Notably, the 4–1 exhibits larger error bars compared to the pristine system, indicating a broader distribution of M-O bond lengths, a hallmark of more severe lattice distortion effects. We quantified this distortion by calculating the average atomic radial displacement (Å) and lattice mismatch δ(%) [71]. In the 4–1 system, the radial displacements for metal and oxygen atoms are 0.075 and 0.221, respectively, both exceeding those of the pristine 0.051 and 0.072. The oxygen atoms, in particular, show a more significant shift. Consistently, the lattice mismatch δ(%) of the 4–1 system (5.734) is considerably larger than that of the pristine system (2.573).

Previous studies have reported that the exceptional radiation resistance of $MgAl_2O_4$ originates from its unique internal structure, in which a large number of intrinsic vacancies provide pathways for cation rearrangement under irradiation. Sickafus and Soeda *et al.* investigated

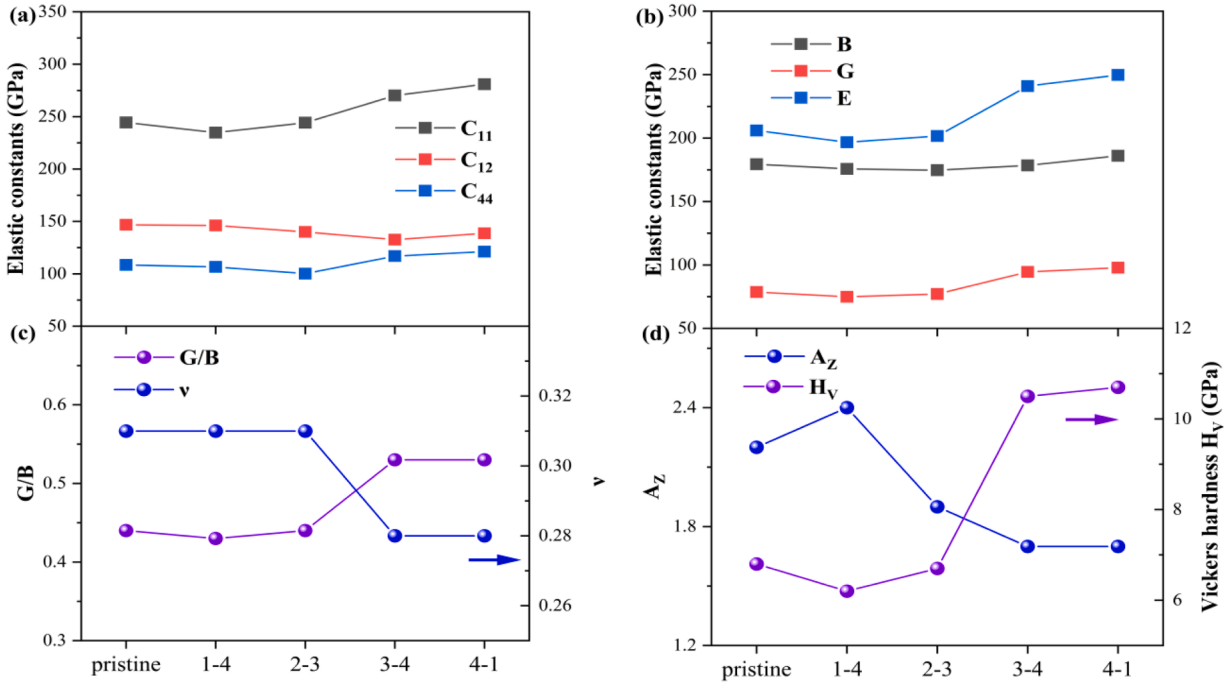

Fig. 7. Influence of the degree of disorder on the mechanical response of HESO (Short name was explained in Table 1). a Elastic constants C_{11}, C_{12}, C_{44}. b Moduli B, G, E. c Poisson's and Pugh's ratios. d Hardness H_V and Zener anisotropy index A_Z.

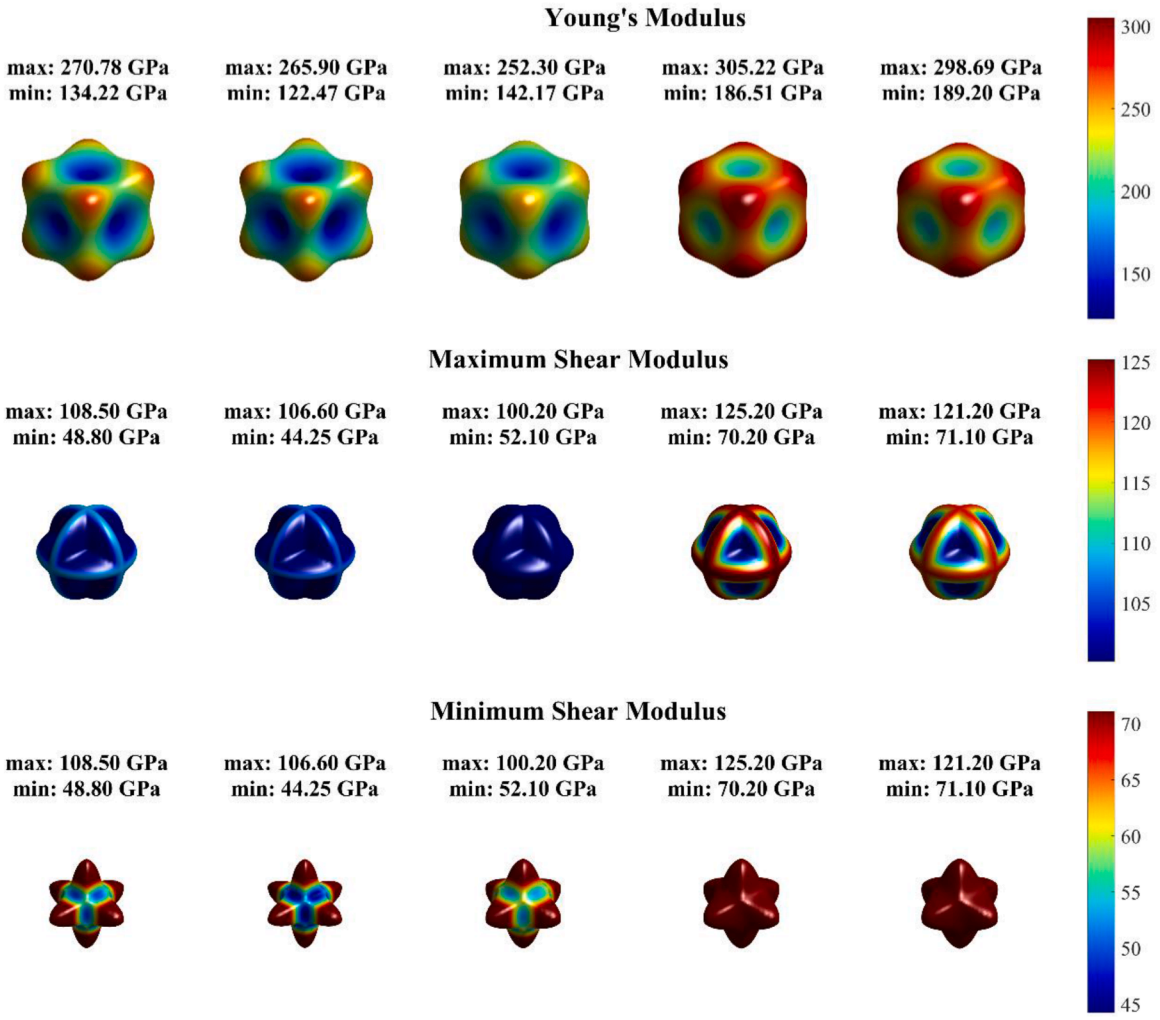

Fig. 8. The spatial distribution of Young's modulus (E), along with the maximum (G_{max}) and minimum (G_{min}) shear moduli of high-entropy spinels (the degree of inversion progressively increases: from left to right are pristine, 1–4, 2–3, 3–4, and 4–1.).

the ion-beam irradiation effects of non-stoichiometric $MgO{\cdot}3(Al_2O_3)$ and $MgO{\cdot}2.4(Al_2O_3)$ spinels [14,29,30]. Under elevated temperature conditions (873 K), vacancy migration was found to be particularly active, and $MgO{\cdot}2.4(Al_2O_3)$ exhibited superior radiation tolerance. These findings highlight the crucial role of vacancy defects in governing the radiation response of spinel structures. Inspired by these observations, we calculated the migration energy barriers of Al vacancies in both the pristine HESO and $MgAl_2O_4$, as shown in Fig. 6. The vacancy migration energies were calculated using the climbing-image nudged elastic band (CI-NEB) method [72] with a force convergence criterion of 0.03 eV/Å. The vacancy migration energy is defined by Eq. (15),

$$E_m^{vacancy} = E_{saddle} - E_d \tag{15}$$

where E_{saddle} denotes the energy of saddle configuration, E_d is defined as the total energy of a stable configuration with a vacancy. The data reveals that the Al vacancy migration barriers in the A-site high-entropy spinel exhibit a broad distribution, reflecting the chemically complex local environments in high-entropy systems. In this work, the migration pathway of an Al vacancy was modeled as hopping from one *16d* site to a nearest-neighbor *16d* site [73]. The Al vacancy migration energy barrier exhibits significant anisotropy. The calculated average migration barrier of Al vacancies in the high-entropy spinel (1.38 eV) is lower than that of MAS (1.61 eV). This result indicates that Al vacancies migrate more readily in the high-entropy system, facilitating efficient recombination of vacancies with interstitials. This enhanced defect recombination potentially improves the amorphization resistance of the material.

3.3. Mechanical properties

The elastic constants of spinel materials were calculated to elucidate the effects of high configurational entropy and cation disorder on their mechanical behavior, in comparison with single-component spinels. Table 3 compares the detailed calculation results with relevant computational and experimental references. Obviously, all studied structures satisfy the mechanical stability condition.

The calculated C_{11}, C_{12}, and C_{44} of $MgAl_2O_4$ follow the established physical trend ($C_{11} > C_{12} > C_{44}$) and demonstrate excellent agreement with previously reported theoretical and experimental data [69,76], thereby validating the accuracy of our computational methodology. Among the single-component spinels, $ZnAl_2O_4$ shows the maximum Young's modulus (265.4 GPa) and Vickers hardness (11.8 GPa) due to its strong internal bonding, while $MnAl_2O_4$ exhibits the lowest modulus but the best ductility. These findings, presented here for the first time, highlight the pronounced compositional sensitivity of the mechanical properties in spinels. For the pristine, 1–4, and 2–3 configurations, which are investigated here for the first time, the calculated C_{11} constants (244.4 GPa, 234.7 GPa, and 244.2 GPa, respectively) are notably lower than those of the single-component spinels (248.3–286.3 GPa), indicating reduced stiffness along the principal axes. Their C_{12} and C_{44} constants, however, remain within the characteristic ranges of these

Table 4
The values of E_{max}, E_{min}, G_{max}, and G_{min}, and the anisotropic descriptors of A_E and A_G of high-entropy spinels.

	E_{max} (GPa)	E_{min} (GPa)	A_E	G_{max} (GPa)	G_{min} (GPa)	A_G
Pristine	271	134	2.02	109	49	2.22
1-4	266	122	2.18	107	44	2.43
2-3	252	142	1.77	100	52	1.92
3-4	288	183	1.57	117	69	1.70
4-1	299	183	1.63	121	71	1.70

single-component systems. Furthermore, the bulk (B), shear (G), and Young's (E) moduli for these novel configurations are lower than those of $ZnAl_2O_4$, $MnAl_2O_4$, and $MgAl_2O_4$. This behavior is attributed to a substantial decrease in C_{11} caused by the weakening of bonds due to specific atomic arrangements along the principal axes, a common effect that has been observed in other ceramics [77]. The Pugh's ratio (k) and Poisson's ratio (ν) are often used to assess the ductility of materials [78]. Generally, a material is considered ductile if ν<0.26 and k(G/B) >0.57 [79]. The Pugh's ratio and Poisson's ratio of pristine are comparable to that of $MnAl_2O_4$, indicating good ductility. This is further supported by the Cauchy pressure (C_{12}-C_{44}), which also suggests ductile behavior [80]. The calculated Vickers hardness (H_v) of pristine is 6.8 GPa, identical to that of $MnAl_2O_4$, and lower than those of the other single-component spinels.

As the degree of antisite disorder increases, distinct trends emerge in the mechanical response of the high-entropy spinel, as shown in Fig. 7a. With increasing disorder, C_{11} first decreases slightly and then continuously increases, reaching a maximum of 280.9 GPa at full disorder, indicating enhanced resistance to axial strain. C_{12} generally decreases but slightly recovers at complete disorder, although it remains lower than the pristine maximum value (146.8 GPa). C_{44} exhibits a non-monotonic change, attaining a maximum of 121.2 GPa at full disorder Fig. 7b further illustrates the impact of disorder on the moduli in the high-entropy system. In $MgAl_2O_4$, disorder increases the bulk modulus and shear modulus [81], and indeed, this also occurs in HES. The bulk modulus B slightly decreases in the case of mild disorder (1–4) and moderate disorder (2–3), but increases significantly under high disorder (3–4 and 4–1), exceeding that of pristine (179.4 GPa) and reaching its maximum value (186.1 GPa) at inverse spinel (4–1). The shear modulus G remains almost unchanged in mild and moderate disorder but increases significantly under high disorder, reaching its maximum value (97.8 GPa) at 4–1, an increase of approximately 24.3 %. Similarly, Young's modulus E follows the same trend as shear modulus G, initially slightly decreasing and then significantly increasing, reaching its maximum value (249.8 GPa) at 4–1, an increase of approximately 21.3 %. Figure 7(c) shows the variation of Pugh's ratio (k) and Poisson's ratio (ν) with increasing antisite defects. As the degree of disorder increases, ductility initially remains stable and then decreases. This is also reflected in the Poisson's ratio, which remains constant (0.31) for mild to moderate disorder but significantly decreases (0.28) under high disorder, indicating a reduction in ductility. Figure 7(d) depicts the variation of Vickers hardness and anisotropy with antisite defect density. The hardness increases significantly under high disorder, which is consistent with the increases in E and G. As the disorder degree increases, the anisotropy generally decreases (except for a slight increase in 1–4).

Overall, the degree of disorder significantly impacts the mechanical

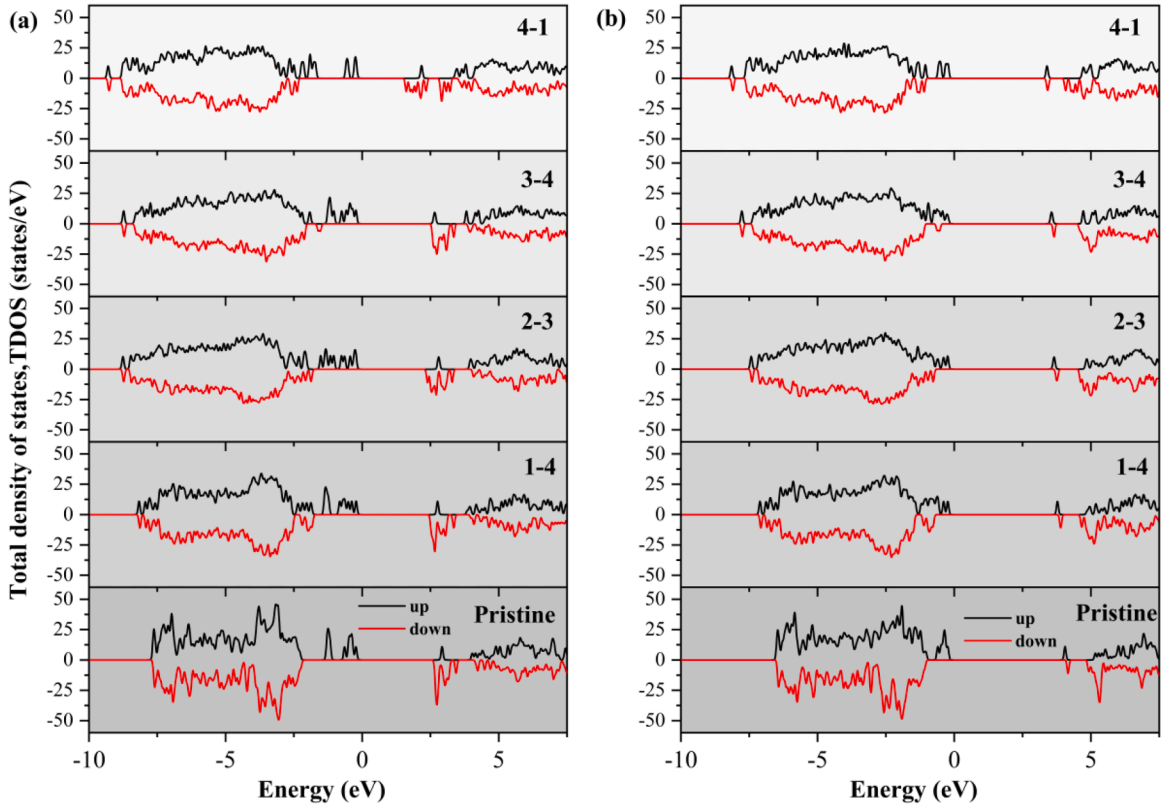

Fig. 9. Density of states analysis for high-entropy spinels with degree of disorder (the degree of inversion progressively increases: from bottom to top are pristine, 1–4, 2–3, 3–4, and 4–1. short name was explained in Table 1). The Fermi level is set to zero for clarity. (a) Results obtained without the Hubbard U correction and (b) results with an effective Hubbard parameter U_{eff} =3.9 applied to the Mn *3d* orbitals.

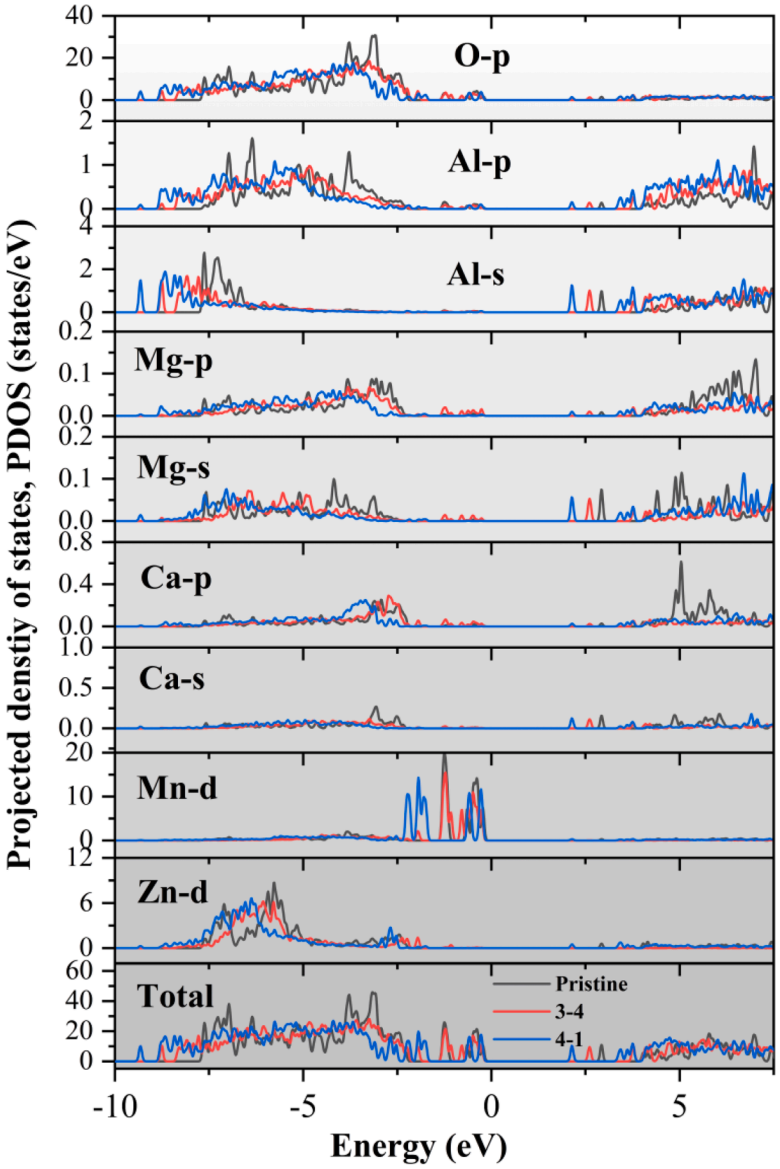

Fig. 10. Projected density of states (PDOS) analysis for high-entropy spinels with degree of disorder. The Fermi level is set to zero for clarity.

performance of high-entropy spinels. Notably, under high disorder (3–4 and 4–1), the material becomes harder and stiffer (with significant increases in G, E, and H_v) but less ductile, as reflected by the increased G/B ratio, decreased Poisson's ratio, and reduced Cauchy pressure. In the case of mild to moderate disorder (1–4 and 2–3), the changes in mechanical properties are negligible, and ductility remains high. The marked decrease in Cauchy pressure under high disorder suggests a shift toward stronger covalent bonding, likely responsible for the observed hardness enhancement. Interestingly, the highly disordered configurations exhibit mechanical properties comparable to or even surpassing those of $MgAl_2O_4$, highlighting the potential of cation antisite engineering to tailor the mechanical robustness of spinel oxides.

Elastic anisotropy is a critical factor influencing microcrack propagation, which is of paramount importance for determining the suitability of materials in practical engineering applications [77]. Given the cubic symmetry of the spinel structure (space group *Fd*-3*m*), elastic anisotropy plays a critical role in determining mechanical response under multiaxial loading. The three-dimensional distributions of Young's modulus (E), maximum shear modulus (G_{max}), and minimum shear modulus (G_{min}) for configurations with varying degrees of disorder are presented in Fig. 8. These surfaces deviate significantly from spherical symmetry, confirming the inherent elastic anisotropy of the spinel lattice. Moreover, the deviation of the Zener ratio (A_z) from 1 provides additional quantitative evidence of this anisotropy [82]. For high-entropy spinel, as the degree of disorder increases, the three-dimensional elastic surfaces gradually approach spherical symmetry, indicating that the material's anisotropy gradually diminishes. This suggests a direct correlation between the reduction in anisotropy and the increasing internal disorder within the spinel.

Analysis of the directional elastic response reveals distinct anisotropic behavior in the high-entropy spinel oxides. Along the principal crystallographic directions, all high-entropy spinels show the highest Young's modulus (E) along the <111> direction and the lowest along the <100> direction. This trend originates from the inherent cubic symmetry (space group Fd-3 m) of the spinel structure, in which the atomic packing density is greatest along the <111> direction, leading to stronger interatomic interactions and, consequently, greater stiffness and resistance to deformation. For the shear response, the maximum shear modulus G_{max} appears along the <100> and <110> directions, indicating enhanced resistance to shear stress in these directions, whereas the minimum value occurs along the <111> direction. The minimum shear modulus G_{min} is largest along the <100> direction and

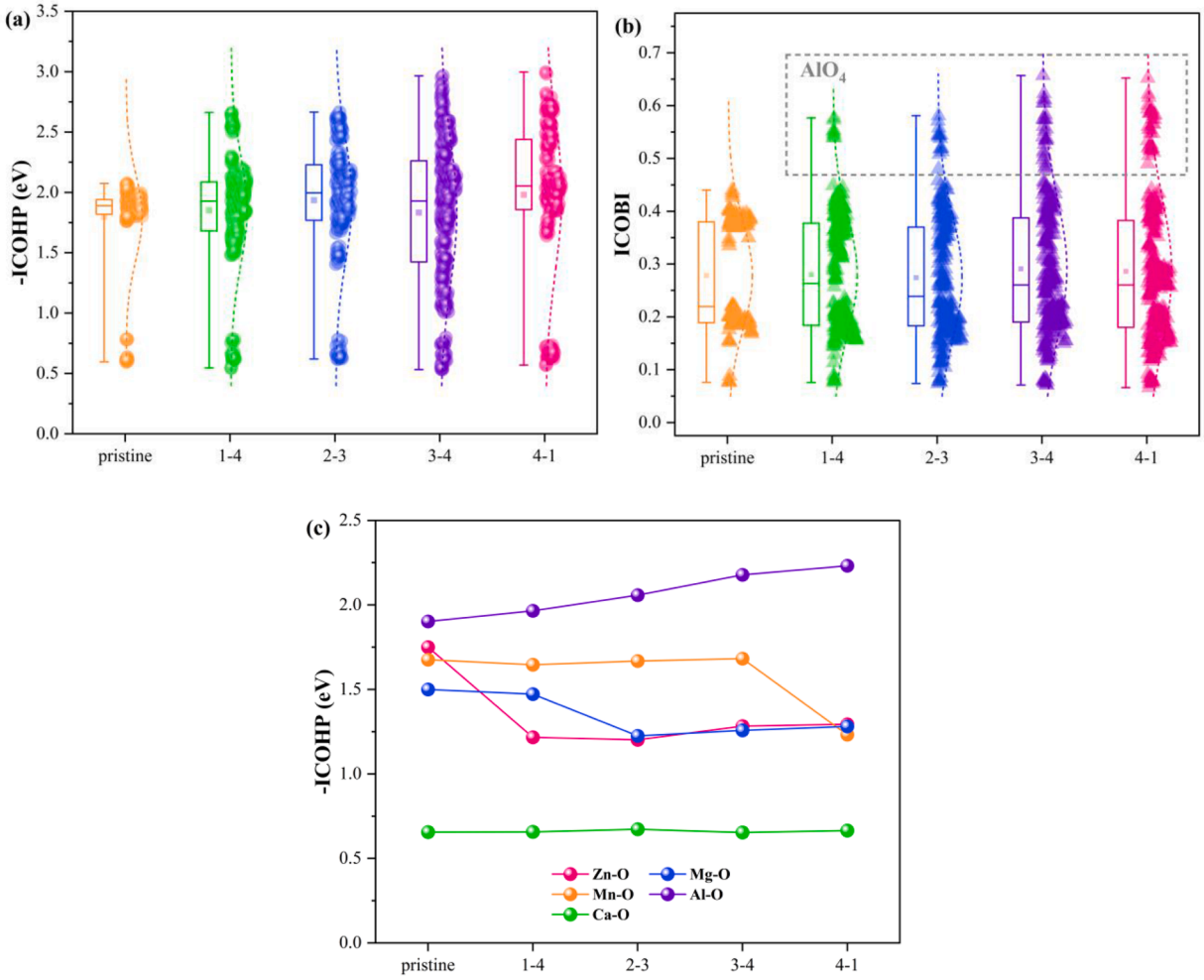

Fig. 11. a Box-plot distribution of negative crystal orbital Hamilton population (-ICOHP) values for M-O bonds in high-entropy spinels, with data points and normal fit curves shown to the right of the boxes. b Integrated Crystal Orbital Bond Index (ICOBI). c Negative crystal orbital Hamilton population (-ICOHP) values for five kinds of M-O bonds with varying degrees of disorder in high-entropy spinels.

smallest along the <110> direction. Notably, along the <100> direction, G_{max} and G_{min} are comparable, indicating that the shear deformation on this plane remains relatively uniform across different shear directions. The elastic anisotropy was further quantified using the ratios $A_E = E_{max}/E_{min}$ and $A_G = G_{max}/G_{min}$, as listed in Table 4. Generally, larger values of these ratios indicate greater anisotropy. With increasing cation disorder, both A_E and A_G decrease to varying extents, confirming that enhanced structural disorder promotes elastic isotropy. Among all configurations, the 3–4 and 4–1 show moduli and overall mechanical performance comparable to those of single-component spinels, yet with markedly reduced anisotropy. This combination of high stiffness and enhanced isotropy suggests that highly disordered high-entropy spinels hold promise for applications requiring mechanically robust and directionally uniform materials.

3.4. Electronic properties

To unravel how antisite defects modify the electronic structure of the high-entropy spinel oxide (HESO), we performed a comprehensive electronic analysis, including total and projected densities of states (TDOS and PDOS) as well as crystal orbital Hamiltonian population (COHP). All COHP calculations were performed using LOBSTER [83–85] code, with all results indicating a charge spilling of less than 5 %. This demonstrates that the projected electronic structures accurately reproduce the original plane-wave results and ensuring the reliability of the bonding analysis.

The TDOS results (Fig. 9) reveal that HESO exhibits semiconducting characteristics with a distinct band gap. As expected, the GGA+U functional yields a larger band gap than standard GGA, which tends to underestimates the value, a well-known limitation of GGA. Importantly, the inclusion of U does not alter the qualitative trends associated with increasing cation disorder. With higher antisite defect densities (2–3, 3–4, and 4–1), the valence band states become more delocalized and broadened, while the sharp TDOS peaks gradually diminish. This indicates that the electronic states evolve from localized “narrow band” states to more delocalized ones due to enhanced orbital hybridization. Such hybridization arises primarily from cation site exchanges, metal cations migrating from tetrahedral to octahedral sites and Al^{3+} ions moving in the opposite direction, which modify the local coordination environments. As a result, M-O covalent interactions are strengthened, and the overall covalency of the system increases at higher disorder levels. This enhanced covalency provides a microscopic explanation for the observed improvement in mechanical properties. According to Gao *et al.*, plastic deformation involves bond breaking followed by bond reformation [86], requiring electron excitation from the valence to the conduction band. The stronger covalent bonding therefore raise the activation energy for such processes, leading to increased hardness and elastic moduli with increasing disorder.

To further clarify the role of transition-metal d electrons in governing covalency, PDOS and COHP analyses were performed for HESOs with

different degrees of antisite disorder, as shown in Fig. 10. The PDOS reveals that the valence band maximum mainly arises from Mn-3d and O-2p hybridization. The bonding region is dominated by strong overlap between O-2p and metal d states, highlighting the covalent nature of M-O bonding. In contrast, Al and Ca contribute minimally to the valence band, reflecting their predominantly ionic bonding with oxygen, consistent with the larger electronegativity differences for Mg-O (2.13) and Ca-O (2.44) compared to Zn-O (1.79) and Mn-O (1.89). The projected density of states (PDOS) reveals distinct hybridization behaviors of Zn and Mn with O-2p states depending on their coordination environments. Consequently, the M-O covalency is substantially enhanced in the tetrahedral environment compared to the octahedral one, which is consistent with the COHP analysis (Fig. 11c). Stronger M-O covalency has also been observed for the tetrahedral-site cation and oxygen ligand pairs in other spinel oxides, leading to the stabilization of their molecular orbitals [87]. Specifically, the average -ICOHP values confirm this viewpoint: Mn-O bonds decrease from 1.68 eV/bond in the tetrahedral sites to 1.32 eV/bond in the octahedral sites, while Zn-O bonds reduce from 1.75 eV/bond to 1.29 eV/bond. Interestingly, Al-O bonds exhibit the opposite trend. When Al^{3+} migrates from octahedral to tetrahedral sites, its s and p states shift toward lower energies, and their DOS peaks broaden-indicative of stronger Al-O hybridization. The -ICOHP values increase from 1.90 eV/bond (octahedral) to 2.23 eV/bond (tetrahedral), confirming enhanced covalency. In contrast, the coordination change has only a minor effect on Mg and Ca. For Mg, the Mg-2p DOS peak slightly decreases, and the Mg-O covalency weakens slightly, with the average -ICOHP value dropping from 1.50 eV/bond in tetrahedral sites to 1.28 eV/bond in octahedral sites. For Ca, both the DOS distribution and the -ICOHP values remain almost unchanged, around 0.66 eV/bond, indicating negligible covalency variation. Although most A-site cations except Ca show reduced M-O covalency when moving into octahedral coordination, the dominant contribution of Al-O bonds leads to an overall enhancement of covalency in the system. This observation is consistent with other results [88] based on bond-valence theory, which demonstrated that Al occupying tetrahedral sites forms stronger covalent bond (Al^{IV}-O) than Zn^{IV}-O, thereby enhancing the overall covalent character of mixed-cation spinels. The enhanced covalency further suggests material hardening, consistent with our Vickers hardness calculations.

The recently developed crystal orbital bond index (COBI) provides an intuitive framework for quantifying covalency in solid-state materials [89]. The integrated COBI (ICOBI) values for all HESOs range from 0.136 to 0.622, confirming the coexistence of ionic and covalent interactions (Fig. 11b). With increasing disorder, the ICOBI distribution exhibits more high values (highlighted within the gray box in Fig. 11b), reflecting the increased presence of Al-O covalent bonds in tetrahedral sites. This enhancement of covalency outweighs the weakening effect of A-site cations occupying octahedral sites, leading to improved mechanical performance at high disorder levels.

Cation antisite disorder has been experimentally observed in complex oxides under irradiation [26,67,90–93]. In $MgAl_2O_4$ spinel, for example, neutron diffraction measurements revealed that under high-flux neutron irradiation, the cation sublattices of A-site (Mg) and B-site (Al) become nearly fully disordered [11]. Similarly, in the HESO systems examined here, increasing internal disorder strengthens the bonding network and enhances mechanical robustness, suggesting that such materials possess great potential for use in extreme irradiation environments.

4. Conclusions

First-principles calculations were employed to investigate the structural stability and intrinsic properties of the A-site high-entropy spinel $(Zn_{0.25}Mn_{0.25}Ca_{0.25}Mg_{0.25})Al_2O_4$ across various cation configurations. The composition exhibits thermodynamic stability, confirmed by its negative formation energy and favorable Gibbs free energy changes of relevant synthesis reactions, from which a feasible solid-state synthesis temperature was derived. Compared with $MgAl_2O_4$, the high-entropy spinel shows a higher average cation antisite defect formation energy but a lower Al-vacancy migration barrier, implying stronger resistance to amorphization and enhanced vacancy mobility. Increasing disorder—characterized by higher configurational entropy and inversion—leads to improved elastic modulus and hardness, alongside reduced anisotropy. These mechanical enhancements are closely linked to the strengthening of M-O bond covalency, mainly driven by the migration of Al^{3+} ions into tetrahedral sites, which increases the overall covalent character of the lattice. This study elucidates the structure-property relationships of Al-based A-site high-entropy spinels and highlights disorder-induced strengthening mechanisms. The results offer guidance for the design of high-entropy oxides with superior mechanical and structural stability, particularly for applications under extreme environments.

CRediT authorship contribution statement

Haowen Guo: Writing – original draft, Formal analysis, Investigation. **Xiaoyi Xia:** Formal analysis. **Yuntao Yang:** Formal analysis. **Chenguang Liu:** Writing – review & editing, Supervision, Resources, Funding acquisition, Formal analysis, Conceptualization. **Qing Peng:** Formal analysis, Writing – review & editing. **Yuhong Li:** Formal analysis, Writing – review & editing. **Fei Gao:** Formal analysis, Writing – review & editing.

Declaration of competing interest

The authors declare that they have no known competing financial interests or personal relationships that could have appeared to influence the work reported in this paper.

Acknowledgments

This work is supported by Shandong Provincial Natural Science Foundation (Grant No. ZR2024MA065), the National Natural Science Foundation of China (Grant No. 12205248) and the start-up fund from Yantai University to C.L. (Grant No. HD20B02.).

Data availability

Data will be made available on request.

References

[1] B. Lin, D. Zhou, How does the explosive growth of AI affect China's power supply and demand: a scenario simulation based on the LEAP model, Renew. Energy (2025) 124485.
[2] D. Dong, J. Guan, Z. Wang, Y. Wang, Current status and trends of nuclear energy under carbon neutrality conditions in China, Energy 314 (2025) 134253.
[3] K. Yasuda, T. Yamamoto, M. Etoh, S. Kawasoe, S. Matsumura, N. Ishikawa, Accumulation of radiation damage and disordering in $MgAl_2O_4$ under swift heavy ion irradiation: dedicated to Prof. Dr.-Ing. Heinrich Wollenberger on the occasion of his 80th birthday, Int. J. Mater. Res. 102 (9) (2011) 1082–1088.
[4] V. Rondinella, T. Wiss, Materials research on inert matrices: a screening study, J. Nucl. Mater. 274 (1-2) (1999) 47–53.
[5] T. Wiss, Heavy ion induced damage in $MgAl_2O_4$, an inert matrix candidate for the transmutation of minor actinides, Radiat. Meas. 31 (1-6) (1999) 507–514.
[6] F. Clinard Jr, G. Hurley, R. Klaffky, Ceramics for fusion reactor applications, Res. Mech.;(U. K.) 8 (4) (1983).
[7] F. Clinard Jr, Ceramics for fusion applications, Ceram. Int. 13 (2) (1987) 69–75.
[8] W.J. Weber, R.C. Ewing, C. Catlow, T.D. De La Rubia, L.W. Hobbs, C. Kinoshita, A. Motta, M. Nastasi, E. Salje, E. Vance, Radiation effects in crystalline ceramics for the immobilization of high-level nuclear waste and plutonium, J. Mater. Res. 13 (6) (1998) 1434–1484.
[9] L. Wang, T. Liang, Ceramics for high level radioactive waste solidification, J. Adv. Ceram. 1 (3) (2012) 194–203.
[10] N. Yu, R. Devanathan, K.E. Sickafus, M. Nastasi, Radiation-induced phase transformations in $MgAl_2O_4$ spinel, J. Mater. Res. 12 (7) (1997) 1766–1770.

[11] K. Sickafus, A. Larson, N. Yu, M. Nastasi, G. Hollenberg, F. Garner, R. Bradt, Cation disorder in high dose, neutron-irradiated spinel, J. Nucl. Mater. 219 (1995) 128–134.
[12] N. Bordes, L. Wang, R. Ewing, K. Sickafus, Ion-beam induced disordering and onset of amorphization in spinel by defect accumulation, J. Mater. Res. 10 (4) (1995) 981–985.
[13] R.C. Ewing, A. Meldrum, L. Wang, S. Wang, Radiation-induced amorphization, Rev. Mineral. Geochem. 39 (1) (2000) 319–361.
[14] T. Soeda, S. Matsumura, C. Kinoshita, N.J. Zaluzec, Cation disordering in magnesium aluminate spinel crystals induced by electron or ion irradiation, J. Nucl. Mater. 283 (2000) 952–956.
[15] S. Zinkle, C. Kinoshita, Defect production in ceramics, J. Nucl. Mater. 251 (1997) 200–217.
[16] L. Minervini, R.W. Grimes, K.E. Sickafus, Disorder in pyrochlore oxides, J. Am. Ceram. Soc. 83 (8) (2000) 1873–1878.
[17] K. Sickafus, L. Minervini, R. Grimes, J.A. Valdez, M. Ishimaru, F. Li, K.J. Mcclellan, T. Hartmann, Radiation tolerance of complex oxides, Science 289 (5480) (2000) 748–751.
[18] J. Lian, J. Chen, L. Wang, R.C. Ewing, J.M. Farmer, L.A. Boatner, K. Helean, Radiation-induced amorphization of rare-earth titanate pyrochlores, Phys. Rev. B 68 (13) (2003) 134107.
[19] D. Simeone, C. Dodane-Thiriet, D. Gosset, P. Daniel, M. Beauvy, Order–disorder phase transition induced by swift ions in $MgAl_2O_4$ and $ZnAl_2O_4$ spinels, J. Nucl. Mater. 300 (2-3) (2002) 151–160.
[20] K.E. Sickafus, Comment on 'order–disorder phase transition induced by swift ions in $MgAl_2O_4$ and $ZnAl_2O_4$ spinels' by D. Simeone et al, J. Nucl. Mater. 300 (2002) 151–160. Journal of nuclear materials 312(1) (2003) 111-123.
[21] M. Ishimaru, I.V. Afanasyev-Charkin, K.E. Sickafus, Ion-beam-induced spinel-to-rocksalt structural phase transformation in $MgAl_2O_4$, Appl. Phys. Lett. 76 (18) (2000) 2556–2558.
[22] B.P. Uberuaga, M. Tang, C. Jiang, J.A. Valdez, R. Smith, Y. Wang, K.E. Sickafus, Opposite correlations between cation disordering and amorphization resistance in spinels versus pyrochlores, Nat. Commun. 6 (1) (2015) 8750.
[23] F. Clinard Jr, G. Hurley, L. Hobbs, Neutron irradiation damage in MgO, Al_2O_3 and $MgAl_2O_4$ ceramics, J. Nucl. Mater. 108 (1982) 655–670.
[24] B.P. Uberuaga, D. Bacorisen, R. Smith, J. Ball, R. Grimes, A.F. Voter, K. Sickafus, Defect kinetics in spinels: long-time simulations of $MgAl_2O_4$, $MgGa_2O_4$, and $MgIn_2O_4$, Phys. Rev. B—Condens. Matter Mater. Phys. 75 (10) (2007) 104116.
[25] D. Bacorisen, R. Smith, B.P. Uberuaga, K. Sickafus, J. Ball, R. Grimes, Atomistic simulations of radiation-induced defect formation in spinels: $MgAl_2O_4$, $MgGa_2O_4$, and $MgIn_2O_4$, Phys. Rev. B—Condens. Matter Mater. Phys. 74 (21) (2006) 214105.
[26] C. Liu, Y. Li, T. Shi, Q. Peng, F. Gao, Oxygen defects stabilize the crystal structure of $MgAl_2O_4$ spinel under irradiation, J. Nucl. Mater. 527 (2019) 151830.
[27] C.R. Kreller, B.P. Uberuaga, The role of cation ordering and disordering on mass transport in complex oxides, Curr. Opin. Solid State Mater. Sci. 25 (2) (2021) 100899.
[28] R. Perriot, B.P. Uberuaga, R.J. Zamora, D. Perez, A.F. Voter, Evidence for percolation diffusion of cations and reordering in disordered pyrochlore from accelerated molecular dynamics, Nat. Commun. 8 (1) (2017) 618.
[29] K.E. Sickafus, N. Yu, M. Nastasi, Radiation resistance of the oxide spinel: the role of stoichiometry on damage response, Nuclear instruments and methods in physics research section B: beam interactions with, Mater. At. 116 (1-4) (1996) 85–91.
[30] S. Murphy, C. Gilbert, R. Smith, T. Mitchell, R. Grimes, Non-stoichiometry in $MgAl_2O_4$ spinel, Philos. Mag. 90 (10) (2010) 1297–1305.
[31] S. Huang, J. Zhang, H. Fu, Y. Xiong, S. Ma, X. Xiang, B. Xu, W. Lu, Y. Zhang, W. J. Weber, Irradiation performance of high entropy ceramics: a comprehensive comparison with conventional ceramics and high entropy alloys, Prog. Mater. Sci. 143 (2024) 101250.
[32] Y. Zhang, G.M. Stocks, K. Jin, C. Lu, H. Bei, B.C. Sales, L. Wang, L.K. Béland, R. E. Stoller, G.D. Samolyuk, Influence of chemical disorder on energy dissipation and defect evolution in concentrated solid solution alloys, Nat. Commun. 6 (1) (2015) 8736.
[33] K. Jin, C. Lu, L. Wang, J. Qu, W. Weber, Y. Zhang, H. Bei, Effects of compositional complexity on the ion-irradiation induced swelling and hardening in Ni-containing equiatomic alloys, Scr. Mater. 119 (2016) 65–70.
[34] C. Lu, L. Niu, N. Chen, K. Jin, T. Yang, P. Xiu, Y. Zhang, F. Gao, H. Bei, S. Shi, Enhancing radiation tolerance by controlling defect mobility and migration pathways in multicomponent single-phase alloys, Nat. Commun. 7 (1) (2016) 13564.
[35] S. Zhao, Y. Osetsky, A.V. Barashev, Y. Zhang, Frenkel defect recombination in Ni and Ni−containing concentrated solid−solution alloys, Acta Mater. 173 (2019) 184–194.
[36] H. Xiao, S. Zhao, Q. Liu, Y. Li, S. Zhao, F. Luo, Y. Wang, Q. Huang, C. Wang, Point defect properties in high entropy MAX phases from first-principles calculations, Acta Mater. 248 (2023) 118783.
[37] L. Xu, M. Niu, H. Wang, L. Su, H. Gao, L. Zhuang, Response of structure and mechanical properties of high entropy pyrochlore to heavy ion irradiation, J. Eur. Ceram. Soc. 42 (14) (2022) 6624–6632.
[38] C. Quan, Q. Fu, R. Qiu, G. Zhao, C. Xu, Achieving superior radiation tolerance in ceramics via in-situ defect recombination, Nat. Commun. 16 (1) (2025) 10502.
[39] Y. Li, S. Zhao, Z. Wu, Uncovering the effects of chemical disorder on the irradiation resistance of high-entropy carbide ceramics, Acta Mater. 277 (2024) 120187.
[40] A. Connelly, R. Hand, P. Bingham, N. Hyatt, Mechanical properties of nuclear waste glasses, J. Nucl. Mater. 408 (2) (2011) 188–193.
[41] Y. Bai, Y. Liang, J. Bi, B. Cui, Z. Lu, B. Li, Role of carbon vacancies in determining the structural, mechanical, and thermodynamic properties of (HfTaZrNb) C_{1-x} high entropy carbides: a first-principles study, J. Mater. Sci. 59 (40) (2024) 19112–19124.
[42] G. Kresse, J. Furthmüller, Efficient iterative schemes for ab initio total-energy calculations using a plane-wave basis set, Phys. Rev. B 54 (16) (1996) 11169.
[43] G. Kresse, J. Hafner, Ab initio molecular-dynamics simulation of the liquid-metal–amorphous-semiconductor transition in germanium, Phys. Rev. B 49 (20) (1994) 14251.
[44] P.E. Blöchl, Projector augmented-wave method, Phys. Rev. B 50 (24) (1994) 17953.
[45] J.P. Perdew, K. Burke, M. Ernzerhof, Generalized gradient approximation made simple, Phys. Rev. Lett. 77 (18) (1996) 3865.
[46] A. Jain, S.P. Ong, G. Hautier, W. Chen, W.D. Richards, S. Dacek, S. Cholia, D. Gunter, D. Skinner, G. Ceder, Commentary: the materials project: a materials genome approach to accelerating materials innovation, APL Mater. 1 (1) (2013).
[47] A. Van De Walle, M. Asta, G. Ceder, The alloy theoretic automated toolkit: a user guide, Calphad 26 (4) (2002) 539–553.
[48] D.S. Lemons, A. Gythiel, Paul Langevin's 1908 paper``on the theory of brownian motion [``Sur la théorie du mouvement brownien,"CR Acad. Sci.(Paris) 146, 530-533 (1908)], Am. J. Phys. 65 (11) (1997) 1079–1081.
[49] K. Momma, F. Izumi, VESTA: a three-dimensional visualization system for electronic and structural analysis, Appl. Crystallogr. 41 (3) (2008) 653–658.
[50] V. Wang, N. Xu, J.-C. Liu, G. Tang, W.-T. Geng, VASPKIT: a user-friendly interface facilitating high-throughput computing and analysis using VASP code, Comput. Phys. Commun. 267 (2021) 108033.
[51] M. Born, in: On the stability of crystal lattices. I, Mathematical Proceedings of the Cambridge Philosophical Society, Cambridge University Press, 1940, pp. 160–172.
[52] S. Pugh, XCII. Relations between the elastic moduli and the plastic properties of polycrystalline pure metals, Lond. Edinb. Dublin Philos. Mag. J. Sci. 45 (367) (1954) 823–843.
[53] G.N. Greaves, A.L. Greer, R.S. Lakes, T. Rouxel, Poisson's ratio and modern materials, Nat. Mater. 10 (11) (2011) 823–837.
[54] X.-Q. Chen, H. Niu, D. Li, Y. Li, Modeling hardness of polycrystalline materials and bulk metallic glasses, Intermetallics 19 (9) (2011) 1275–1281.
[55] T.-Y. Chen, S.-Y. Wang, C.-H. Kuo, S.-C. Huang, M.-H. Lin, C.-H. Li, H.-Y.T. Chen, C.-C. Wang, Y.-F. Liao, C.-C. Lin, Operando synchrotron X-ray studies of a novel spinel $(Ni_{0.2}Co_{0.2}Mn_{0.2}Fe_{0.2}Ti_{0.2})_3O_4$ high-entropy oxide for energy storage applications, J. Mater. Chem. A 8 (41) (2020) 21756–21770.
[56] A.A. Emery, C. Wolverton, High-throughput DFT calculations of formation energy, stability and oxygen vacancy formation energy of ABO_3 perovskites, Sci. Data 4 (1) (2017) 1–10.
[57] W. Sun, S.T. Dacek, S.P. Ong, G. Hautier, A. Jain, W.D. Richards, A.C. Gamst, K. A. Persson, G. Ceder, The thermodynamic scale of inorganic crystalline metastability, Sci. Adv. 2 (11) (2016) e1600225.
[58] G. Hautier, S.P. Ong, A. Jain, C.J. Moore, G. Ceder, Accuracy of density functional theory in predicting formation energies of ternary oxides from binary oxides and its implication on phase stability, Phys. Rev. B—Condens. Matter Mater. Phys. 85 (15) (2012) 155208.
[59] S.-Y. Liu, C. Liu, S. Zhang, S. Liu, D.-J. Li, Y. Li, S. Wang, Phase diagram and mechanical properties of fifteen quaternary high-entropy metal diborides: first-principles calculations and thermodynamics, J. Appl. Phys. 131 (7) (2022).
[60] S.-Y. Liu, J. Cui, C. Zhang, W. Gong, S. Liu, B. Yu, D. Li, M. Huang, S. Wang, First-principles study on the thermodynamic miscibility and mechanical properties of high-entropy quaternary metal nitrides, Mater. Today Commun. 45 (2025) 112157.
[61] G.K. Nayak, A. Kretschmer, P.H. Mayrhofer, D. Holec, On correlations between local chemistry, distortions and kinetics in high entropy nitrides: an ab initio study, Acta Mater. 255 (2023) 118951.
[62] H. Wang, C. Zhu, C. He, D. Yang, Y. Li, DFT+ U study and in-situ TEM investigation of high-entropy titanate pyrochlore $(Lu_{0.25}Y_{0.25}Eu_{0.25}Gd_{0.25})_2Ti_2O_7$, J. Eur. Ceram. Soc. 42 (16) (2022) 7546–7552.
[63] B. Ye, T. Wen, M.C. Nguyen, L. Hao, C.-Z. Wang, Y. Chu, First-principles study, fabrication and characterization of $(Zr_{0.25}Nb_{0.25}Ti_{0.25}V_{0.25})C$ high-entropy ceramics, Acta Mater. 170 (2019) 15–23.
[64] Y. He, L. Zhang, H.-W. Xiong, K.-C. Zhou, X. Kang, The selective site occupation, structural and thermal stability of high entropy $(CoCrFeMnNi)_3O_4$ spinel, J. Alloys Compd. 965 (2023) 171428.
[65] A. Sarkar, B. Breitung, H. Hahn, High entropy oxides: the role of entropy, enthalpy and synergy, Scr. Mater. 187 (2020) 43–48.
[66] D. Gosset, D. Simeone, M. Dutheil, S. Bouffard, M. Beauvy, Structural evolutions of spinels under ions irradiations, J. Eur. Ceram. Soc. 25 (12) (2005) 2677–2681.
[67] R.I. Sheldon, T. Hartmann, K.E. Sickafus, A. Ibarra, B.L. Scott, D.N. Argyriou, A. C. Larson, R.B. Von Dreele, Cation disorder and vacancy distribution in nonstoichiometric magnesium aluminate spinel, $MgO{\cdot}xAl_2O_3$, J. Am. Ceram. Soc. 82 (12) (1999) 3293–3298.
[68] X. Yang, Y. Zhang, Prediction of high-entropy stabilized solid-solution in multi-component alloys, Mater. Chem. Phys. 132 (2-3) (2012) 233–238.
[69] C. Liu, Y. Lu, Q. Peng, C. Xu, K. Yang, X. Li, D. Su, Y. Li, F. Gao, The effect of Sr doping on the structural, mechanical, electronic properties and radiation tolerance of $MgAl_2O_4$ spinel: a first-principles study, J. Alloys Compd. 889 (2021) 161614.
[70] V. Kocevski, G. Pilania, B.P. Uberuaga, How inversion relates to disordering tendencies in complex oxides, Phys. Chem. Chem. Phys. 25 (40) (2023) 27189–27195.
[71] Y. Bai, Y. Liang, J. Bi, B. Cui, Z. Lu, H. Wang, X. You, B. Li, Sintering, high-temperature stability, and thermal conductivity of (Zr, Nb, Hf, Ta)(C, N) high-entropy carbonitrides, Ceram. Int. 51 (18) (2025) 24731–24739.

[72] B.P.U.G. Henkelman, H. Jónsson, A climbing image nudged elastic band method for finding saddle points and minimum energy paths, J. Chem. Phys. 113 (2000) 9901–9904.
[73] N. Grimes, Self-diffusion in compounds with spinel structure, Philos. Mag. 25 (1) (1972) 67–76.
[74] S. Akbudak, A. Kushwaha, G. Uğur, Ş. Uğur, H.Y. Ocak, Structural, electronic, elastic, optical and vibrational properties of MAl_2O_4 (M= Co and Mn) aluminate spinels, Ceram. Int. 44 (1) (2018) 310–316.
[75] X.-C. Mao, K. Liu, B.-S. Hou, J. Tan, X.-L. Zhou, Theoretical investigation of the structural, elastic, and thermodynamic properties of $MgAl_2O_4$ spinel under high pressure, J. Phys. Soc. Jpn. 85 (11) (2016) 114605.
[76] V. Askarpour, M. Manghnani, S. Fassbender, A. Yoneda, Elasticity of single-crystal $MgAl_2O_4$ spinel up to 1273 K by Brillouin spectroscopy, Phys. Chem. Miner. 19 (8) (1993) 511–519.
[77] B. Liu, H. Zhou, Y. Liu, S. Li, K. Chu, Z. Qu, W. Li, Y. Li, Structural origin of anisotropic mechanical/thermal behavior in $La_2SrAl_2O_7$ and $Nd_2SrAl_2O_7$ perovskites, J. Am. Ceram. Soc. 108 (4) (2025) e20307.
[78] K. Balasubramanian, S.V. Khare, D. Gall, Valence electron concentration as an indicator for mechanical properties in rocksalt structure nitrides, carbides and carbonitrides, Acta Mater. 152 (2018) 175–185.
[79] S.-Y. Liu, S. Zhang, S. Liu, D.-J. Li, Z. Niu, Y. Li, S. Wang, Stability and mechanical properties of single-phase quinary high-entropy metal carbides: first-principles theory and thermodynamics, J. Eur. Ceram. Soc. 42 (7) (2022) 3089–3098.
[80] R. Thompson, W. Clegg, Predicting whether a material is ductile or brittle, Curr. Opin. Solid State Mater. Sci. 22 (3) (2018) 100–108.
[81] L. Li, P. Carrez, D. Weidner, Effect of cation ordering and pressure on spinel elasticity by ab initio simulation, Am. Mineral. 92 (1) (2007) 174–178.
[82] C. Zener, Elasticity and anelasticity of metals, University of Chicago Press, 1965.
[83] R. Dronskowski, P.E. Bloechl, Crystal orbital Hamilton populations (COHP): energy-resolved visualization of chemical bonding in solids based on density-functional calculations, J. Phys. Chem. 97 (33) (1993) 8617–8624.
[84] V.L. Deringer, A.L. Tchougréeff, R. Dronskowski, Crystal orbital Hamilton population (COHP) analysis as projected from plane-wave basis sets, J. Phys. Chem. A 115 (21) (2011) 5461–5466.
[85] R. Nelson, C. Ertural, J. George, V.L. Deringer, G. Hautier, R. Dronskowski, LOBSTER: local orbital projections, atomic charges, and chemical-bonding analysis from projector-augmented-wave-based density-functional theory, J. Comput. Chem. 41 (21) (2020) 1931–1940.
[86] Z. Fang, K. Terakura, Structuraldistortion and magnetism in transition metal oxides: crucialroles of orbital degrees of freedom, J. Phys.: Condens. Matter 14 (11) (2002) 3001.
[87] W. Xie, S.J.H. Ong, Z. Shen, L. Tian, K. Tang, S. Xi, Z.J. Xu, Critical role of tetrahedral coordination in determining the polysulfide conversion efficiency on spinel oxides, J. Am. Chem. Soc. 147 (1) (2024) 988–997.
[88] P. Xu, H. Wang, L. Ren, B. Tu, W. Wang, Z. Fu, Theoretical study on composition-dependent properties of $ZnO{\cdot}nAl_2O_3$ spinels. Part II: mechanical and thermophysical, J. Am. Ceram. Soc. 104 (12) (2021) 6455–6466.
[89] P.C. Müller, C. Ertural, J. Hempelmann, R. Dronskowski, Crystal orbital bond index: covalent bond orders in solids, J. Phys. Chem. C 125 (14) (2021) 7959–7970.
[90] C. Liu, Q. Peng, T. Shi, F. Gao, Y. Li, Physical properties and radiation tolerance of high-entropy pyrochlores Gd2 $(Ti_{0.25}Zr_{0.25}Sn_{0.25}Hf_{0.25})_2O_7$ and individual pyrochlores $Gd_2X_2O_7$ (X= Ti, Zr, Sn, Hf) from first principles calculations, Scr. Mater. 220 (2022) 114898.
[91] U. Schmocker, F. Waldner, The inversion parameter with respect to the space group of $MgAl_2O_4$ spinels, J. Phys. C: Solid State Phys. 9 (9) (1976) L235.
[92] U. Schmocker, H. Boesch, F. Waldner, A direct determination of cation disorder in $MgAl_2O_4$ spinel by ESR, Phys. Lett. A 40 (3) (1972) 237–238.
[93] G.B. Andreozzi, F. Princivalle, H. Skogby, A.Della Giusta, Cation ordering and structural variations with temperature in $MgAl_2O_4$ spinel: an X-ray single-crystal study, Am. Mineral. 85 (9) (2000) 1164–1171.